Received: 12 December 2017 | Revised: 14 June 2018 | Accepted: 23 July 2018

DOI: 10.1002/bit.26813

ARTICLE

WILEY BIOTECHNOLOGY BIOENGINEERING

Computational fluid dynamic modeling of alternating tangential flow filtration for perfusion cell culture

Flaka Radoniqi[1] | Hu Zhang[1] | Cameron L. Bardliving[1] | Parviz Shamlou[1] | Jon Coffman[2]

[1]School of Applied Life Sciences, Amgen Bioprocessing Center, Keck Graduate Institute, Claremont, California

[2]Department of Process Science, Boehringer Ingelheim, Fremont, California

Correspondence
Flaka Radoniqi, Amgen Bioprocessing Center, Keck Graduate Institute, 535 Watson Drive, Claremont 91711, CA.
Email: fradon14@students.kgi.edu

Abstract

Alternating tangential flow (ATF) filtration has been successfully adopted as a low shear cell separation device in many perfusion-based processes. The reverse flow per cycle is used to minimize fouling compared with tangential flow filtration. Currently, modeling of the ATF system is based on empirically derived formulas, leading to oversimplification of model parameters. In this study, an experimentally validated porous computational fluid dynamic (CFD) model was used to predict localized fluid behavior and pressure profiles in the ATF membrane for both water and supernatant solutions. The results provided numerical evidence of Starling flow phenomena that has been theorized but not previously proven for the current operating parameters. Additionally, feed cross flow velocity was shown to significantly impact the localized flux distribution; higher feed cross flow rates lead to an increased localized permeate flux as well as irreversible and reversible fouling resistance. Further, the small average permeate flux values of 2 $L \cdot m^{-2} \cdot h^{-1}$ traditionally used in perfusion bioreactor membranes lead to approximately 50% of the membrane length utilized for permeate flow during each pressure and exhaust phase, leading to a full membrane utilization during one ATF cycle. Our preliminary CFD results demonstrate that local flux and resistance distribution further elucidate the dynamics of ATF membrane fouling in a perfusion-based system.

KEYWORDS

alternating tangential flow filtration, computational fluid dynamics, cross flow velocity, Starling flow

1 | INTRODUCTION

Perfusion bioreactors are currently the subject of much research because of their potential for continuous processing and commercial production of therapeutic proteins and antibodies yielding a consistent product quality (Pollock, Coffman, Ho, & Farid, 2017; Rodrigues, Costa, Henriques, Azeredo, & Oliveira, 2009; Su, 2009; Warikoo et al., 2012; Zydney, 2016). Several technologies have been developed for perfusion systems but microfiltration-based tangential flow filtration (TFF) and alternating flow filtration (ATF) are technologies of choice for cell separation in perfusion bioreactors since they have shown to be robust in supporting very high cell densities in perfusion cell culture (Clincke, Mölleryd, Zhang, et al., 2013).

In a typical perfusion bioreactor, cell suspension is pumped continuously through a hollow fiber either in TFF or in an ATF system to separate the spent media containing the protein of interest from cells. The spent media (permeate) is forward processed to purify the protein product while the cells are returned to the bioreactor where

fresh media is added to replace the spent media. The ATF system (Repligen, Waltham, MA) is unique in that a diaphragm pump and control system serve to generate alternating flow through the hollow fiber module, instead of unidirectional flow as operated in the TFF system. During the pressure phase, the air chamber of the diaphragm is pressurized and pushes liquid through the hollow fibers, into the reactor. This is followed by an exhaust phase where air leaves the chamber though the means of a vacuum pump, pushing the liquid back into the diaphragm liquid chamber (Chotteau, 2015).

The hollow fiber-based perfusion bioreactor has many advantages that are well-documented (Godawat, Konstantinov, Rohani, & Warikoo, 2015; Konstantinov et al., 2006; Langer & Rader, 2014; Meier et al., 2014). Nevertheless, one major drawback that is limiting its widespread adoption is membrane fouling and product retention (Clincke, Mölleryd, Samani, et al., 2013; Karst, Serra, Villiger, Soos, & Morbidelli, 2016; Kim et al., 2016; Wang et al., 2017). Product retention is a particularly important phenomenon for stable operation and refers to the ability of the membrane to maintain the desired protein product concentration in permeate and retentate streams. However, often because of membrane fouling, retention of the protein product over time increases in the retentate stream leading to loss of process control and potentially loss of product quality.

Concentration polarization and membrane fouling determinately affect product retention. The former is a reversible, caused by protein build-up at the membrane surface. The latter is irreversible and is generally associated with the build-up of cells, cell debris, particulate, and extracellular material at the membrane surface and/or within its pores (Belfort, Davis, & Zydney, 1994; Field, 2010).

A lot of research has been focused on characterization of the ATF system performance as a cell retention device and comparisons to the TFF have demonstrated superiority of ATF in terms of low shear and reduced fouling and retention of the product (Clincke, Mölleryd, Samani, et al., 2013; Karst, Serra, et al., 2016; Wang et al., 2017). In the exhaust cycle of the ATF system, there is the potential for reverse flow across the membrane, which is thought to minimize fouling, possibly due to flow back into the lumen near the exit fiber. This is known as Starling recirculation phenomenon and is thought to be responsible for the removal of deposited material (Zydney, 2016).

Multiple models are available to describe irreversible membrane fouling leading to flux decline. These include resistance in series models based on protein adsorption, pore plugging, and surface deposition models. However, only a few researchers have focused on characterization of fouling in the ATF system (Kelly et al., 2014). Additionally, in each case proper validation of the model requires detailed information about structural properties of the membrane including its thickness, pore size, size distribution, and porosity as well as local flow conditions, including for example, axial and radial flow velocities and pressure drops in the bulk region and close to walls of the lumen. Oftentimes, local flow information is not available leading to gross oversimplification of model parameters. It has also previously been shown that cell culture supernatant contributes to fouling of the membrane, independent of the cell suspension (Wang et al., 2017). This provided the motivation for the work reported in this publication to use computational fluid dynamics (CFD) to study flow of cell culture supernatant through porous membrane in an ATF system. This is the first step toward creating predictive models for membrane fouling and sieving decline to guide process design and optimization of the hollow fiber-based ATF system.

2 | MATERIALS AND METHODS

2.1 | Experimental studies

A small-scale perfusion bioreactor system was used for all experiments reported in this study. An in-house recombinant monoclonal antibody-producing Chinese Hamster Ovary (CHO) cell line from Boehringer Ingelheim Pharmaceuticals Inc. (Fremont, CA) was cultured in a 2-L perfusion bioreactor for 29 days. The peak cell density was maintained at ~30 million cells/ml beginning at Day 10. Cell culture supernatant was harvested and collected on Day 29 at a cell viability of 75%. The cell culture was then centrifuged at 243 rcf for 20 min (CS-6R; Beckman Coulter, Brea, CA) to separate cells and larger debris from supernatant. Previously, Wang et al. (2017) showed that protein sieving was not impacted after the membranes were exposed to permeate solution that had already passed through a 0.2-μm membrane or solution containing cell pellet resuspended in permeate. However, when cell culture supernatant containing primarily particles in the 100-nm size range was introduced to a new hollow fiber membrane, product sieving was severe and almost instantaneous.

Experiments were conducted using the ATF 2 H and C-24 controller system equipped with a polysulfone (PS) membrane (S02-P20Y-10-S; Spectrum Labs, Rancho Dominguez, CA) containing 75 lumens and a membrane surface area of 470 cm^2. The membranes pore size distribution was a nominal average of 0.2 μm and the lumens were 20-cm long with an ID of 1 mm. Membrane (i.e., lumen wall) thickness was measured to be ~140 μm using a Hitachi SU-70 Scanning Electron Microscope (Hitachi High-Technologies, Chatsworth, CA). A new membrane was used for each experiment with no pretreatment.

Figure 1 outlines a schematic of the ATF set-up. A reservoir containing 250 ml of water or cell culture supernatant was recirculated through the membrane cartridge and returned to the reservoir at various cross flow velocities (Table 1). The ATF cycle time for different cross flow velocities was calculated using the following relationship:

$$\text{Cycle time (min)} = \frac{\text{Pump displacement volume (L)}}{\text{Flow rate (L/min)}}. \quad (1)$$

The reservoir was kept at a constant volume by recirculating the retentate and permeate into the feed reservoir. A constant permeate flux of 2 $L{\cdot}m^{-2}{\cdot}h^{-1}$ was maintained using a peristaltic pump (114 DV; Watson Marlow, Wilmington, MA). SciPress single-use pressure sensors (SciLog, Madison, WI) were placed at the inlet, outlet, and permeate lines to monitor pressure change during cycles, as shown in Figure 1. The pressure values were recorded by a SciPress pressure monitor (accuracy ±0.02 psi) and the data was collected with the SciPress data acquisition software every second. A flow meter (Leviflow, LFSC-D

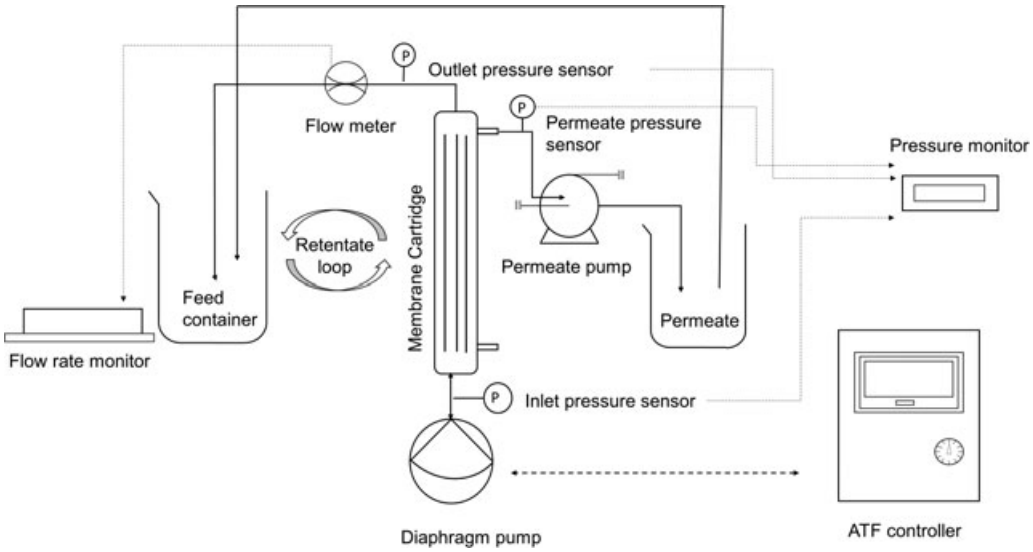

FIGURE 1 Schematic drawing of a small-scale ATF perfusion-based system studied in the present work. ATF: alternating tangential flow

series; Levitronix, Zürich, Switzerland) was placed at the outlet line of the hollow fiber cartridge to record flow rate change during pressure and exhaust cycles. The flow rate values were read and collected by a levitronix dynamic controller system (accuracy ±1%).

The hydraulic filtration resistances were measured based on established methods (Hwang & Sz, 2011; Stressmann & Moresoli, 2008) and calculated using Darcy's equation below:

$$J = \frac{\mathrm{TMP}}{\mu R_t} = \frac{\mathrm{TMP}}{\mu\left(R_m + R_{rev} + R_{irev}\right)}, \quad (2)$$

where J is permeate flux (m/s), TMP is transmembrane pressure (kg/m s^2), μ is filtrate viscosity (kg/m s), R_t (m^{-1}) is total membrane resistance during operation, R_{rm} (m^{-1}) is intrinsic membrane resistance, R_{rev} (m^{-1}) is reversible fouling resistance, and R_{irev} (m^{-1}) is irreversible fouling resistance. The clean membrane resistance, R_m, was obtained by flowing deionized water through the membrane at a set TMP value. The obtained R_m value was used as an input parameter for CFD simulations using water. For supernatant experiments, total membrane resistance, R_t, during the last hour of operation (6 hr) was calculated and used as an input parameter for CFD simulations using supernatant. When an experiment was terminated, the supernatant feed was switched to deionized water. The filtration resistance caused by reversible fouling, R_{rev}, was obtained from the difference between the total filtration resistance before and after feed switch. The resistance caused by irreversible membrane fouling, R_{irr}, was then calculated by subtracting the other resistances from the total filtration resistance. R_{rev} and R_{irr} values were used to compare the impact of different operating conditions on membrane resistance change.

Switching from process fluid to water for measuring membrane permeability may cause precipitation of dissolved species and result in fouling. We observed membrane fouling only under certain conditions using supernatant solution. However, fouling was not observed when switching to water as a feed after the membranes were exposed to protein solution or media. Therefore, water was used as a fluid switch for measuring hydraulic resistances.

2.2 | CFD simulations

All CFD simulations modeled a single porous fiber under the assumption that the inlet and permeate mass flow rate was equally distributed among the fibers. Figure 2 shows a two-dimensional (2D) axisymmetric single-fiber model that was generated using ANSYS FLUENT version 18.2 (ANSYS Inc., Canonsburg, PA). The model consisted of a lumen,

TABLE 1 Experimental parameters and conditions used for the ATF studies

Solution	ATF cycle time (s)	Cartridge cross flow rate (L·m^{-1})	Fiber permeate flux (L·m^{-2}·h^{-1})	Fiber cross flow velocity (m·s^{-1})	Avg. permeate flow rate/fiber (ml·min^{-1})
Cell culture supernatant	29.7	0.4	2	0.11	0.021
	14.9	0.8	2	0.22	0.021
	7.9	1.5	2	0.70	0.021
Water	29.7	0.4	2	0.11	0.021
	14.9	0.8	2	0.22	0.021
	7.9	1.5	2	0.70	0.021

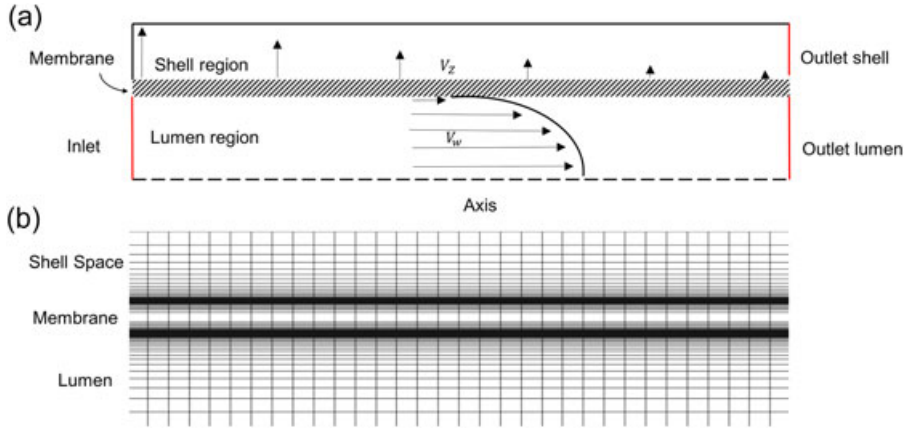

FIGURE 2 Geometry and computational mesh used for the CFD simulations of a single fiber in the ATF system. (a) 2D axisymmetric representation of the fiber with inlet, outlet shell, and outlet lumen as boundary conditions (in red). Axis location is designated by dashed line. (b) Zoomed view of fiber mesh. Dark regions represent mesh refinement along the membrane edge. ATF: alternating tangential flow; CFD: computational fluid dynamic; 2D: two-dimensional

membrane, and shell domain shown in Figure 2a. A 433,357 element quadrilateral mesh was used for the 2D fiber (Figure 2b). The mesh density was chosen based on mesh independence study where higher resolution at the membrane boundary provided the most accurate results, validated experimentally.

A transient laminar single-phase model was designed to model alternating flow in the fiber. The fluid was assumed to be Newtonian and incompressible. Viscous fluid flow is governed by the basic principles of the continuity and Navier–Stokes equations, which can be written in cylindrical coordinates as

$$\frac{\partial_{v_r}}{\partial_r}+\frac{v_r}{r}+\frac{\partial_{v_z}}{\partial_z}=0, \tag{3}$$

$$\rho v_r\frac{\partial v_r}{\partial_r}+\rho v_z\frac{\partial v_z}{\partial_z}+\frac{\partial P}{\partial_r}-\frac{\partial}{\partial_r}\left(2\mu\frac{\partial v_r}{\partial_r}\right)-2\mu\frac{\partial v_r}{\partial_r}+2\mu\frac{v_r}{r^2}-\frac{\partial}{\partial_z}\left[\mu\left(\frac{\partial v_z}{\partial_r}+\frac{\partial v_r}{\partial_z}\right)\right]-\rho g_r=0, \tag{4}$$

$$\rho v_r\frac{\partial v_z}{\partial_r}+\rho v_z\frac{\partial v_z}{\partial_z}+\frac{\partial P}{\partial_z}-\frac{\partial}{\partial_z}\left(2\mu\frac{\partial v_z}{\partial_z}\right)-\frac{\mu}{r}\left(\frac{\partial v_z}{\partial_r}+\frac{\partial v_r}{\partial_z}\right)-\frac{\partial}{\partial_r}\left[\mu\left(\frac{\partial v_z}{\partial_r}+\frac{\partial v_r}{\partial_z}\right)\right]-\rho g_z=0, \tag{5}$$

where p is the density of the fluid ($kg{\cdot}m^{-3}$), ν *is* the fluid velocity ($m{\cdot}s^{-1}$) with r and z representing the radial and axial coordinates (m), respectively, μ is the fluid velocity (Pa s), P is the pressure (Pa), and g is the acceleration due to gravity ($m{\cdot}s^{-2}$; Ghidossi, Veyret, & Moulin, 2006; Keir & Jegatheesan, 2014). The SIMPLE pressure–velocity coupling algorithm with second-order upwind discretization scheme for momentum and pressure were used. The convergence criteria for momentum and continuity was selected to be 10^{-4}. The model was run transiently according to the pump cycle time for each cross flow velocity condition (Table 1).

A time-dependent velocity profile boundary condition was set at the inlet of the fiber. Velocity profile with respect to time was computed from the feed flow rates measured experimentally by a flow meter at the ATF outlet for one cycle (Table 1). The fluid flow was assumed to be equally distributed in all of the hollow fibers, therefore the cartridge mass flow rate was scaled down to one fiber (dividing by 75 fibers) and the velocity profile was calculated by dividing volumetric flow rate by fiber cross-sectional area. The outlet boundary of the fiber was set to atmospheric pressure. The shell boundary condition was set by assuming a uniform distribution of permeate flux through all fibers. The shell average velocity was $2.55\times10^{-4}\ m{\cdot}s^{-1}$, and calculated based on shell area and permeate mass flow rate. The shell average velocity corresponds to a permeate flux of $2\ L{\cdot}m^{-2}{\cdot}h^{-1}$.

The porous region of the lumen was modeled using a resistance value captured from experimental hydraulic resistances described previously, and a porosity of 0.65 obtained from the manufacturer. The permeate flux distribution was then a function of resistance and transmembrane pressure differences between the lumen side and the shell side. The local permeate flux was calculated based on the radial component of velocity.

3 | RESULTS AND DISCUSSION

3.1 | Validation of the CFD model

Previously, ATF has been modeled using a series of empirically derived equations where important parameters such as local velocity, pressure drop, and permeate flux are lumped into single average values (Kelly et al., 2014). The CFD approach presented in this study provided the basis for improved understanding of the impact of operating conditions on factors such as product sieving (Wang et al., 2017) and membrane utilization (Stressmann & Moresoli, 2008). A 2D axisymmetric CFD model was developed using experimental membrane resistance as an input for the simulations. Average inlet pressure and permeate pressure during one cycle were used as outputs to validate the model against experimental data. Root mean square error analysis show a good agreement between the experimental and CFD outputs (Table 2).

TABLE 2 Root mean square error (RMSE) difference between experimental and CFD model

Cross flow velocity ($m \cdot s^{-1}$)	Avg. water inlet pressure (psi)	Avg. water permeate pressure (psi)
0.11	0.04	0.02
0.22	0.11	0.05
0.70	0.19	0.12

Figure 3 shows further validation of the CFD model against experimental profiles of pressure over one cycle (exhaust and pressure phase). It can be observed in Figure 3a that the simulated inlet pressure profile closely resembles the experimental profile across the cycle and is consistent across a range of feed cross flow velocities. Figure 3b shows the CFD and experimental permeate pressure profile across one cycle. As was observed with the inlet pressure profile predictions, the permeate pressure profile also showed good agreement with the CFD model using water as the fluid. As shown in Figure 3, it can be concluded that the simplified single-fiber CFD model correctly predicts inlet and permeate pressure profiles of hollow fiber cartridge axially and temporally.

3.2 | Flow and pressure pattern in the ATF system

The ATF system has several advantages over the TFF system, and has been used in numerous perfusion processes (Clincke, Mölleryd, Zhang, et al., 2013; Karst, Steinebach, Soos, & Morbidelli, 2016; Kelly et al., 2014). However recent studies have shown that product sieving is not improved with ATF under certain conditions (Wang et al., 2017). CFD model of the complex spatial and temporal variations in pressure and permeate flow in these systems may provide additional insight and understanding of how operational parameters can affect product sieving for perfusion bioreactors.

Figure 4 shows water flow axially and radially (colored according to the velocity magnitude) at inlet, center, and outlet regions of the fiber at a feed cross flow velocity of 0.11 $m \cdot s^{-1}$ during a single time point (10 s) of pressure phase. Figure 4a shows the single fiber used in the computational domain, representing the flow for the entire cartridge. Figure 4b shows the predicted laminar flow profile in the center region of the lumen. The model predicts Starling flow occurring in the middle region (10 cm) of the membrane depicted by a change in direction of the radial velocity (as shown by the change in the arrow directions). Figure 4c elucidates the mechanism for Starling flow in the porous membrane as the result of variations in transmembrane pressure differences between the lumen and the shell zone as predicted in literature (Starling, 1896).

As shown in Figure 4c for the imposed conditions, approximately half of the membrane is utilized for permeate flow during each pressure and exhaust phase of the cycle. Current CFD results show that the percent membrane utilization is not sensitive to changes in the feed cross flow rate values in the range of 0.11–0.70 $m \cdot s^{-1}$ at the very low permeate flux of 2 $L\,m^{-2} \cdot h^{-1}$. However, other CFD simulations (data not shown here) showed that once permeate flux was increased from 2 to 15 $L\,m^{-2} \cdot h^{-1}$, membrane utilization increased from 50% to 70%, respectively. This may indicate that membrane utilization is a function of the ratio of feed cross flow rate and permeate flux.

While half membrane utilization would persist in tangential flow under these conditions, in the ATF system the bidirectional flow allows for full membrane utilization per cycle. This may explain the improved performance of ATF over TFF under these operating conditions. Figure 5 shows spatial and temporal distribution of Starling flow for 0.11, 0.22, and 0.7 $m \cdot s^{-1}$ feed cross flow velocities

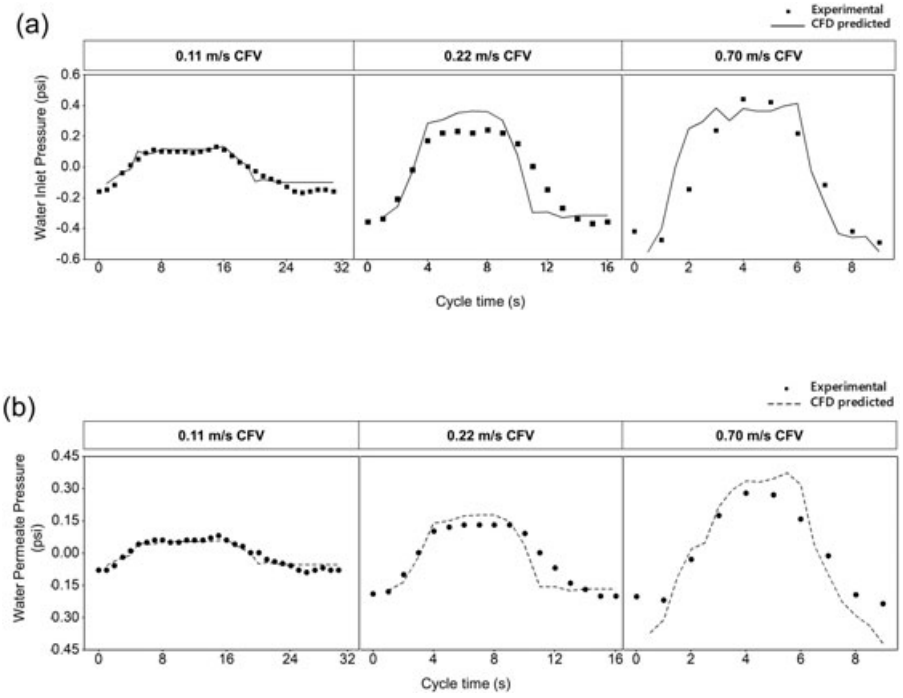

FIGURE 3 Comparison of CFD simulated and experimental water inlet pressure profile (a) and water permeate pressure profile (b) during one ATF cycle at feed cross flow velocities (CFV) of 0.11, 0.22, and 0.7 $m \cdot s^{-1}$. CFD inlet boundary condition was expressed as a velocity distribution measured experimentally with a flow meter over one cycle. Outlet lumen was set to 0 Pa. Permeate flow rate was kept constant at 0.000255 $m \cdot s^{-1}$ which is equivalent to permeate flux of 2 $L \cdot m^{-2} \cdot h^{-1}$. ATF: alternating tangential flow; CFD: computational fluid dynamic

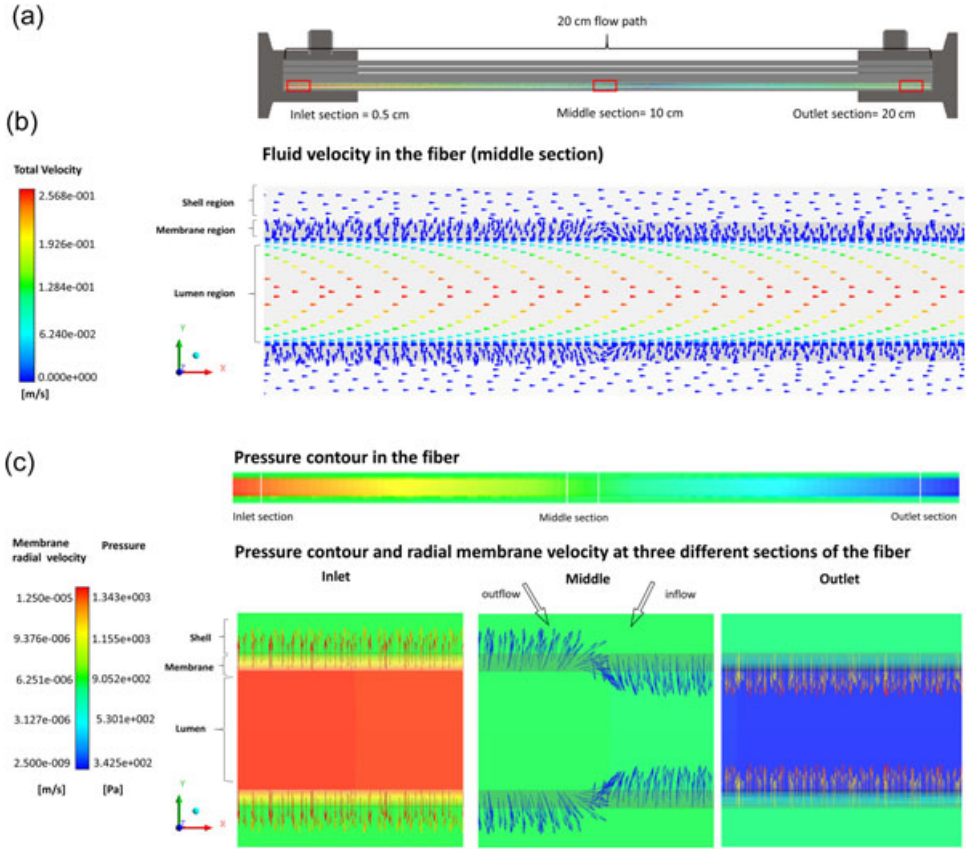

FIGURE 4 Fluid flow dynamics in the ATF-based hollow fiber membrane at 0.11 m·s^{-1} CFV at 10 s time point of pressurized phase. (a) A computer-generated sketch of a hollow fiber cartridge showing a colored single fiber used as computational domain for all CFD simulations. (b) Velocity flow field of a section of a single hollow fiber. (c) Multiple sections (inlet, center, and outlet) of membrane velocity overlaid on transmembrane pressure contour. Starling flow phenomenon is driven by axial variations in transmembrane pressure differences between the lumen zone and the shell zone. ATF: alternating tangential flow; CFD: computational fluid dynamic

(panels a, b, and c) at an average permeate velocity of 2.55×10^{-4} m·s^{-1}. Although membrane utilization is the same for all conditions, local permeate flux across the membrane at the entrances is lower at 0.11 m·s^{-1} feed cross flow velocity (Figure 5a) compared with feed cross flow velocities of 0.22 m·s^{-1} (Figure 5b) and of 0.70 m·s^{-1} (Figure 5c), where an increase in magnitude was ~2- and ~4-fold, respectively. During each pressure and exhaust phase, the total permeate mass flow through the membrane increases with higher feed cross flow velocity (Table 3 and Figure 5d), as a consequence of higher TMP (data not shown here).

Previous attempts at modeling microfiltration systems have primarily focused on understanding the fluid dynamics of within the lumen region. Figueredo-Cardero, Martínez, Chico, Castilho, and Medronho (2014) used a CFD model for a perfusion-based rotating cylindrical filter and inferred the presence of Starling flow based on the pressure differences at the filter surface. However, the authors' model did not include the porous region of the lumen and as a result did not show flux distribution. To the best of our knowledge, this is the first time that Starling flow phenomenon has been demonstrated and quantified in a porous membrane in the ATF system using CFD.

3.3 | Effects of supernatant solution on pressure profiles and membrane resistance

Day 29 centrifuged CHO cell culture supernatant was recirculated through the ATF system for 6 hr at a range of feed cross flow velocities (0.11–0.70 m·s^{-1}) to simulate the impact of peak protein concentrations on the performance of ATF. The CFD-simulated permeate pressure profiles were calculated at the outlet shell boundary region. Figure 6 shows the CFD and experimental permeate pressure profile across one cycle. The root mean square error (RMSE) between the experimental and CFD predicted values were 0.05, 0.10, and 0.16 for feed cross flow velocity conditions of 0.11, 0.22, and 0.70 m·s^{-1}, respectively, indicating a good agreement between predicted and observed values.

To gain insight into the impact of supernatant solution properties on different filtration resistances, intrinsic membrane resistance (R_m), total membrane resistance (R_t), reversible fouling resistance (R_{rev}), and irreversible fouling resistance (R_{rev}) were estimated using Darcy's equation. As shown in Figure 7, clean membrane resistance remained constant for all conditions (5.00×10^{10} m^{-1}). Reversible and irreversible fouling membrane resistances were the highest for the

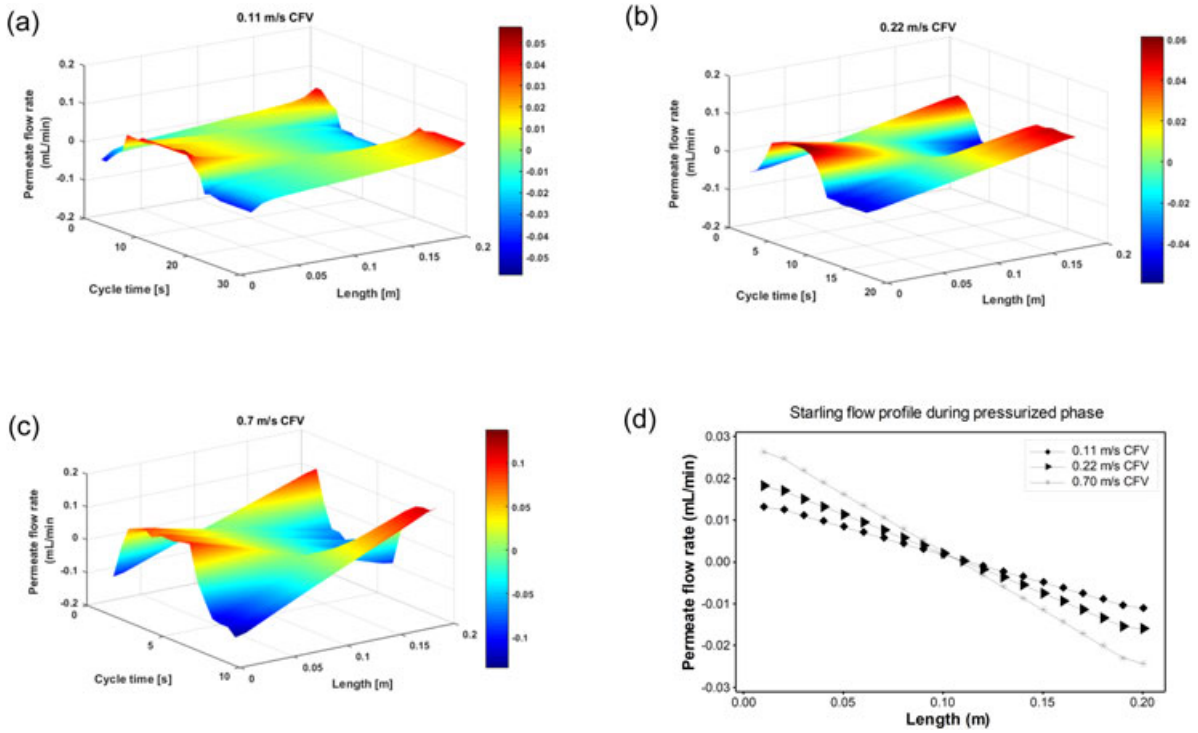

FIGURE 5 Permeate flow distribution axially and temporally at feed cross flow velocities (CFV) of (a) 0.11 m·s^{-1}, (b) 0.22 m·s^{-1}, and (c) 0.7 m·s^{-1}. Highest and lowest permeate value are depicted in red and blue color, respectively. Membrane volumetric flow rate as a function of position along the lumen for various feed cross flow rates (d). A similar membrane utilization of 50% is seen across both phases and is consistent between the feed cross flow rates examined. CFD inlet boundary condition was expressed as a velocity derived experimentally. Outlet lumen was set to 0 Pa and outlet shell boundary condition was set to a 0.00255 m·s^{-1} velocity equivalent to 2 L m^{-2}·h^{-1}. CFD: computational fluid dynamic

TABLE 3 Distribution of permeate flux during one cycle at different cross flow velocities

		Pressurized phase			Exhaust phase		
Feed Solution	Cross flow velocity (m·s^{-1})	Outflow (ml·min^{-1})	Inflow (ml·min^{-1})	Avg. Permeate flow rate (ml·min^{-1})	Outflow (ml·min^{-1})	Inflow (ml·min^{-1})	Avg. Permeate flow rate (ml·min^{-1})
Water	0.11	0.077	0.056	0.021	0.053	0.032	0.021
	0.22	0.151	0.130	0.021	0.121	0.100	0.021
	0.70	0.190	0.170	0.021	0.180	0.159	0.021

Note. Outflow: permeate flow out of the lumen; inflow: permeate flow back into the lumen.

membrane exposed to 0.70 m·s^{-1} feed cross flow velocity followed by 0.22 and 0.11 m·s^{-1} feed cross flow rate. Stressmann and Moresoli (2008) showed a similar trend with supernatant solution and a membrane operating under the constant flux mode. These observations may not be intuitively obvious as high shear stress applied to the liquid at the membrane surface reduces the cake layer build-up and could be considered beneficial in reducing membrane fouling (Silva, Reeve, Husain, Rabie, & Woodhouse, 2000). However, Taddei, Aimar, Howell, and Scott (2007) suggested the compaction of the material already deposited on the membrane might be less susceptible to the shear forces provided by a higher feed cross flow velocity. Additionally, Stressmann and Moresoli (2008) calculated the initial fouling rate to be high at higher feed cross flow velocities, suggesting increased interactions between the feed components and the membrane. This hypothesis may be supported by the current CFD results showing an approximately 4 to 9-fold increase in permeate outflow in high cross flow velocity condition when compared with the average permeate flow rate (Table 3 and Figure 5d).

As shown by previous studies (Wang et al., 2017), low cell culture viabilities result in an increase in particle size in the 100-nm range that affects membrane permeability and product sieving. These data suggest that operating within moderate feed cross flow velocities 0.11–0.22 m·s^{-1} might be advantageous in reducing permeate flow gradient, and potentially minimizing the fouling incidence by particles in the 100-nm size range. It is important to note that for these simulations, an average total membrane resistance was assumed. However, since the permeate flow distribution changes temporally and spatially, it may be the case that fouling distribution also varies.

Several empirical models developed for feed cross flow filtration suggest that bidirectional flow and/or Starling flow contribute to

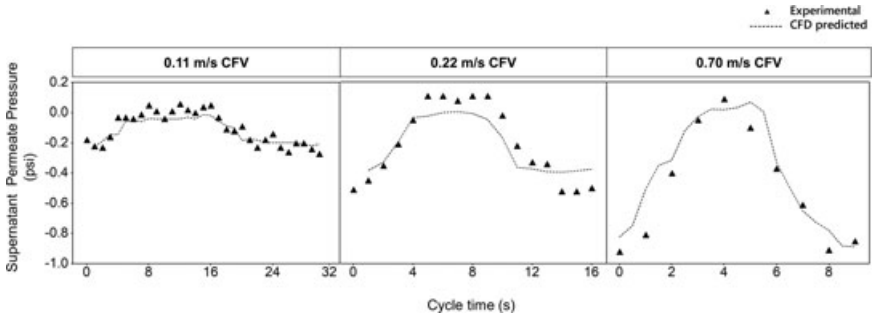

FIGURE 6 Comparison of simulated supernatant permeate pressure profile with experimentally measured profile during one ATF cycle with the experimental data at feed cross flow velocities (CFV) of 0.11, 0.22, and 0.7 $m \cdot s^{-1}$. Supernatant solution was obtained from the last day of perfusion cell culture. Total resistance was calculated at the last hour of operation was used for supernatant CFD simulations. Permeate flow rate was kept constant at 0.000255 $m \cdot s^{-1}$ which is equivalent to a permeate flux of 2 $L \cdot m^{-2} \cdot h^{-1}$. ATF: alternating tangential flow; CFD: computational fluid dynamic

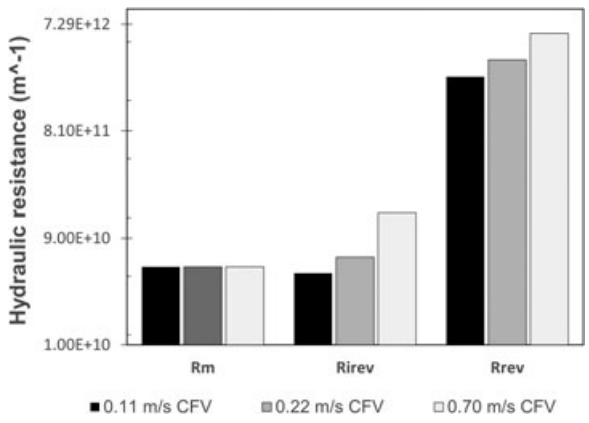

FIGURE 7 Comparison of different filtration resistances of hollow fiber membrane in ATF system under different feed cross flow velocities. R_m is intrinsic membrane resistance, R_{rev} is reversible fouling resistance, and R_{irev} is irreversible fouling resistance. Higher feed cross flow velocity conditions increase R_{rev} and R_{irev} resistances compared with lower feed cross flow velocities. ATF: alternating tangential flow

cleaning the membrane surface during operation (Breslau, Testa, Milnes, & Medjanis, 1980; Schulz & Ripperger, 1989). However, our current data show that Starling flow did not minimize membrane fouling as the feed cross flow velocity increased. This may imply that the bidirectional flow behavior is a more important aspect for ATF operation leading to a full membrane utilization per cycle.

In addition to operating conditions and bioreactor environment, hollow fiber length might play a major role in distribution of permeate flux. Binabaji, Ma, Rao, and Zydney (2016) investigated the effects of fiber length on the ultrafiltration of monoclonal antibody solution. The authors found that the pressure drop increased with increasing fiber length, leading to an increase in back-filtration and a reduction in antibody maximum concentration. These findings highlight the importance of fiber length on TMP drop and thus permeate flux distribution, posing a challenge in hollow fiber scale up in perfusion bioreactors. Taken together, current and previous studies suggest that the localized flux distribution might play a major role in membrane fouling rate at the current operating conditions.

4 | CONCLUSION

A CFD model was developed and validated to describe the complex flow in the lumen of an ATF system. Simulations accurately showed the transient fluid flow and pressure profiles in the ATF system with highly permeable membranes, such as those used in the perfusion processes. Starling flow phenomena, which has been hypothesized to occur, was confirmed and quantified with the use of the CFD model. The present work provided numerical evidence of Starling flow and the effect of different operational conditions on distribution of localized permeate flux.

The results obtained clearly indicate that flux in the high-pressure side of the cartridge is increased when a feed cross flow rate is high, due to a higher TMP. CFD simulations of Starling flow using water showed approximately half utilization of the membrane during each pressure and exhaust phase, leading to a full membrane utilization per cycle. The CFD model also predicted flux and pressure profile for cell culture supernatant flowing in the lumen. Membrane exposed to supernatant solution at a high feed cross flow velocity was associated with highest reversible and irreversible fouling resistance.

This is the first step in developing a design space for optimal parameters including feed cross flow rate and TMP. These preliminary CFD results suggest that an improved fouling model should take into account local flux and resistance distribution to better understand the impact of different operating conditions on fouling and sieving of membranes in an ATF perfusion-based system.

ACKNOWLEDGMENTS

The authors are grateful for the Bioprocess Engineering group at Boehringer Ingelheim Inc. (Fremont, CA) for their support on this project. The authors thank Samantha Wang, Arash Abedijaberi, Raquel Orozco, and Scott Godfrey for their support on the execution of the ATF experimental and modeling studies.

ORCID

Flaka Radoniqi http://orcid.org/0000-0003-0162-0925

REFERENCES

Belfort, G., Davis, R. H., & Zydney, A. L. (1994). The behavior of suspensions and macromolecular solutions in crossflow microfiltration. *Journal of Membrane Science*, *96*, 1–58. https://doi.org/.org/10.1016/0376-7388(94)00119-7

Binabaji, E., Ma, J., Rao, S., & Zydney, A. L. (2016). Ultrafiltration of highly concentrated antibody solutions: Experiments and modeling for the effects of module and buffer conditions. *Biotechnology Progress*, *32*(3), 692–701. https://doi.org/.org/10.1002/btpr.2252

Breslau, B. R., Testa, A. J., Milnes, B. A., & Medjanis, G. (1980). Advances in hollow fiber ultrafiltration technology, *Ultrafiltration membranes and applications* (109–127). Boston, MA: Springer US. https://doi.org/.org/10.1007/978-1-4613-3162-9_7

Chotteau, V. (2015). Perfusion processes. In Al-Rubeai, M. (Ed.), *Animal cell culture* (pp. 407–443). Switzerland: Springer. https://doi.org/.org/10.1007/978-3-319-10320-4_13

Clincke, M. F., Mölleryd, C., Samani, P. K., Lindskog, E., Fäldt, E., Walsh, K., & Chotteau, V. (2013). Very high density of Chinese Hamster Ovary cells in perfusion by alternating tangential flow or tangential flow filtration in WAVE bioreactor TM— Part II: Applications for antibody production and cryopreservation. *Biotechnology Progress*, *29*, 768–777. https://doi.org/10.1002/btpr.1703

Clincke, M. F., Mölleryd, C., Zhang, Y., Lindskog, E., Walsh, K., & Chotteau, V. (2013). Very high density of CHO cells in perfusion by ATF or TFF in WAVE bioreactor. Part I: Effect of the cell density on the process. *Biotechnology Progress*, *29*(3), 754–767. https://doi.org/10.1002/btpr.1704

Field, R. (2010). Fundamentals of fouling. In Peinemann, K.-V., & Nunes, S. Pereira (Eds.), *Membrane technology* (1st ed., 4, *pp. 1–23). Weinheim, Germany: Wiley-VCH Verlag GmbH & Co. KGaA. pp. https://doi.org/.org/10.1002/9783527631407.ch1*

Figueredo-Cardero, A., Martínez, E., Chico, E., Castilho, L. R., & Medronho, R. A. (2014). Rotating cylindrical filters used in perfusion cultures: CFD simulations and experiments. *Biotechnology Progress*, *30*(5), 1093–1102. https://doi.org/10.1002/btpr.1945

Ghidossi, R., Veyret, D., & Moulin, P. (2006). Computational fluid dynamics applied to membranes: State of the art and opportunities. *Chemical Engineering and Processing: Process Intensification*, *45*(6), 437–454. https://doi.org/10.1016/J.CEP.2005.11.002

Godawat, R., Konstantinov, K., Rohani, M., & Warikoo, V. (2015). End-to-end integrated fully continuous production of recombinant monoclonal antibodies. *Journal of Biotechnology*, *213*, 13–19. https://doi.org/10.1016/j.jbiotec.2015.06.393

Hwang, K.-J., & Sz, P.-Y. (2011). Effect of membrane pore size on the performance of cross-flow microfiltration of BSA/dextran mixtures. *Journal of Membrane Science*, *378*(1–2), 272–279. https://doi.org/10.1016/j.memsci.2011.05.018

Karst, D. J., Serra, E., Villiger, T. K., Soos, M., & Morbidelli, M. (2016). Characterization and comparison of ATF and TFF in stirred bioreactors for continuous mammalian cell culture processes. *Biochemical Engineering Journal*, *110*, 17–26. https://doi.org/10.1016/j.bej.2016.02.003

Karst, D. J., Steinebach, F., Soos, M., & Morbidelli, M. (2016). Process performance and product quality in an integrated continuous antibody production process. *Biotechnology and Bioengineering*, *114*(2), 298–307. https://doi.org/10.1002/bit.26069

Keir, G., & Jegatheesan, V. (2014). A review of computational fluid dynamics applications in pressure-driven membrane filtration. *Reviews in Environmental Science and Biotechnology*, *13*(2), 183–201.

Kelly, W., Scully, J., Zhang, D., Feng, G., Lavengood, M., Condon, J., … Bhatia, R. (2014). Understanding and modeling alternating tangential flow filtration for perfusion cell culture. *Biotechnology Progress*, *30*(6), 1291–1300. https://doi.org/10.1002/btpr.1953

Kim, S. C., An, S., Kim, H. K., Park, B. S., Na, K. H., & Kim, B. G. (2016). Effect of transmembrane pressure on Factor VIII yield in ATF perfusion culture for the production of recombinant human Factor VIII co-expressed with von Willebrand factor. *Cytotechnology*, *68*(5), 1687–1696. https://doi.org/10.1007/s10616-015-9918-1

Konstantinov, K., Goudar, C., Ng, M., Meneses, R., Thrift, J., Chuppa, S., … Naveh, D. (2006). The "push-to-low" approach for optimization of high-density perfusion cultures of animal cells. *Advances in Biochemical Engineering/ Biotechnology*, *101*, 75–98.

Langer, E. S., & Rader, R. A. (2014). Continuous bioprocessing and perfusion: Wider adoption coming as bioprocessing matures. *BioProcess Journal*, *13*, 43–49. https://doi.org/10.12665/J131.Langer

Meier, K., Carstensen, F., Scheeren, C., Regestein, L., Wessling, M., & Büchs, J. (2014). In situ product recovery of single-chain antibodies in a membrane bioreactor. *Biotechnology and Bioengineering*, *111*(8), 1566–1576. https://doi.org/10.1002/bit.25220

Pollock, J., Coffman, J., Ho, S. V., & Farid, S. S. (2017). Integrated continuous bioprocessing: Economic, operational, and environmental feasibility for clinical and commercial antibody manufacture. *Biotechnology Progress*, *33*(4), 854–866. https://doi.org/10.1002/btpr.2492

Rodrigues, M. E., Costa, A. R., Henriques, M., Azeredo, J., & Oliveira, R. (2009). Technological progresses in monoclonal antibody production systems. *Biotechnology Progress*, *26*, 332–351. https://doi.org/10.1002/btpr.348

Schulz, G., & Ripperger, S. (1989). Concentration polarization in crossflow microfiltration. *Journal of Membrane Science*, *40*(2), 173–187. https://doi.org/10.1016/0376-7388(89)89003-9

Silva, C. M., Reeve, D. W., Husain, H., Rabie, H. R., & Woodhouse, K. A. (2000). Model for flux prediction in high-shear microfiltration systems. *Journal of Membrane Science*, *173*(1), 87–98. https://doi.org/10.1016/S0376-7388(00)00355-0

Starling, E. H. (1896). On the absorption of fluids from the connective tissue spaces. *The Journal of Physiology*, *19*(4), 312–326. https://doi.org/10.1113/jphysiol.1896.sp000596

Stressmann, M., & Moresoli, C. (2008). Effect of pore size, shear rate, and harvest time during the constant permeate flux microfiltration of CHO cell culture supernatant. *Biotechnology Progress*, *24*(4), 890–897. https://doi.org/10.1021/bp.4

Su, W. W. (2009). Bioreactors, perfusion, *Encyclopedia of Industrial Biotechnology* (1–17). Hoboken: John Wiley & Sons, Inc. https://doi.org/10.1002/9780470054581.eib149

Taddei, C., Aimar, P., Howell, J. A., & Scott, J. A. (2007). Yeast cell harvesting from cider using microfiltration. *Journal of Chemical Technology & Biotechnology*, *47*(4), 365–376. https://doi.org/10.1002/jctb.280470407

Wang, S., Godfrey, S., Ravikrishnan, J., Lin, H., Vogel, J., & Coffman, J. (2017). Shear contributions to cell culture performance and product recovery in ATF and TFF perfusion systems. *Journal of Biotechnology*, *246*, 52–60. https://doi.org/10.1016/j.jbiotec.2017.01.020

Warikoo, V., Godawat, R., Brower, K., Jain, S., Cummings, D., Simons, E., … Konstantinov, K. (2012). Integrated continuous production of recombinant therapeutic proteins. *Biotechnology and Bioengineering*, *109*(12), 3018–3029. https://doi.org/10.1002/bit.24584

Zydney, A. L. (2016). Continuous downstream processing for high value biological products: A Review. *Biotechnology and Bioengineering*, *113*(3), 465–475. https://doi.org/10.1002/bit.25695

How to cite this article: Radoniqi F, Zhang H, Bardliving CL, Shamlou P, Coffman J. Computational fluid dynamic modeling of alternating tangential flow filtration for perfusion cell culture. *Biotechnology and Bioengineering*. 2018;115: 2751–2759. https://doi.org/10.1002/bit.26813